

Experimental investigation of a Wells turbine under dynamic stall conditions for wave energy conversion

Michele Stefanizzi^{*}, Sergio Mario Camporeale, Marco Torresi

Department of Mechanics, Mathematics and Management (DMMM), Polytechnic University of Bari, Via Re David 200, 70125, Bari, Italy

ARTICLE INFO

Keywords:

Wells turbine
Wave energy
OWC
Ocean energy
Marine energy
Blue economy

ABSTRACT

Marine energy still plays a marginal role in the current global energy scenario, despite the incessant effort by research for more than thirty years in the exploitation of the so-called blue energy. Among the wide range of marine technologies, wave energy harvesting can play a significant role in view of its potential and Oscillating Water Column (OWC) systems, coupled with Wells turbines, can be considered among the most mature wave energy technology. Due to the oscillating nature of the flow rate in this kind of applications, Wells turbines are affected by dynamic stall, which has significant effects in terms of performance, fatigue, noise and structural integrity of the turbine.

Actually, during dynamic stall, the Wells turbine experiences evident high frequency torque fluctuations which overlay on the typical hysteresis loop, mainly during flow deceleration. The amplitudes of these fluctuations are damped as the flow rate decreases toward reattachment. Often these fluctuations are not evident because hysteresis loops are usually provided with phase-averaged data, which can significantly smoothen or even conceal them. Indeed, it is difficult to find in the literature high frequency torque measurements able to show these fluctuations. With the aim to better investigate how the stall triggers this phenomenon, a monoplane Wells turbine has been manufactured in 3D printing and tested in the open wind tunnel of the Polytechnic University of Bari, Italy. The interest of the experimental campaign has been mainly focused on the effects of main parameters of the oscillating inlet flow rate (mean flow rate, amplitude and period of the oscillations, modifying the controlling parameters of the inverter driving the squirrel cage blower) on the performance of the machine. The machine has been firstly investigated under steady state inlet flow conditions, then under dynamic stall conditions. As a result, unsteady torque fluctuations occur during the flow deceleration till the flow reattachment. After the stall, the investigated Wells turbine experiences a drastic reduction of the torque coefficient of about 90%. Moreover, the torque coefficient shows a number of peaks during deceleration phases ranging from 2 to 4. Specifically, the case with the maximum period of the flow rate under investigation (i.e., $T = 20$ s) shows a greater number of peaks (4) than those related to the other cases (3). Moreover, it has been found that this unsteady behavior is due neither to the mass flow rate crossing the turbine, nor to the stagnation pressure drop, nor to the rotational speed control, which is correctly performed keeping the rotational speed within 1% of the target value. Hence, detecting these oscillations can be relevant in the turbine design phase to enhance the structural strength of the turbine.

1. Introduction

Nowadays the effects of the climate change are so tangible that they can no longer be ignored and direct counter actions cannot be postponed anymore. The widespread adoption of renewables and related technologies represents an essential solution to fight worrisome issues such as energy poverty and energy security. One of the latest report by the International Renewable Energy Agency (IRENA) outlined that CO₂

emissions related to the energy production sector reached a new peak of over 36.8 Gt in 2022 [1]. Despite the sharp trend inversion caused by the COVID-19 pandemic (almost 8% lower than in 2019, i.e. 31.5 Gt CO_{2,eq} in the 2020), global CO₂ emissions due to energy production rebounded in 2021 [2–4]. In this scenario, the recent COP 27 has represented an important milestone, giving a strong signal with an even more explicit desire to global zero net emissions by 2050 and to limit the increase in temperatures to 1.5 °C above pre-industrial levels. In order to achieve

^{*} Corresponding author. Re David 200, 70125, Bari, Italy.

E-mail addresses: michele.stefanizzi@poliba.it (M. Stefanizzi), sergio.camporeale@poliba.it (S.M. Camporeale), marco.torresi@poliba.it (M. Torresi).

<https://doi.org/10.1016/j.renene.2023.05.120>

Received 21 July 2022; Received in revised form 24 April 2023; Accepted 28 May 2023

Available online 10 June 2023

0960-1481/© 2023 The Authors. Published by Elsevier Ltd. This is an open access article under the CC BY license (<http://creativecommons.org/licenses/by/4.0/>).

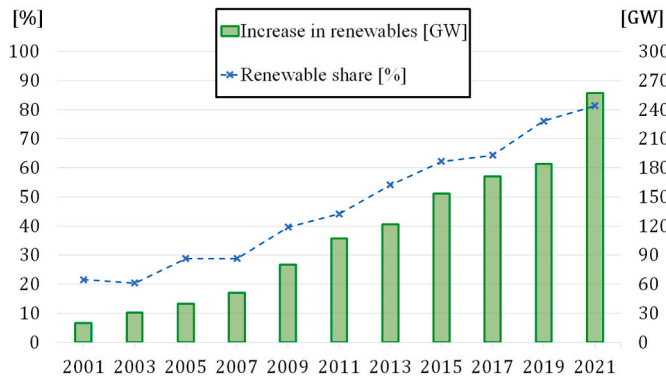


Fig. 1. Trend of share and annual capacity addition of renewable based power.

these ambitious goals, Nations are called to accelerate the phase-out of coal, curtail deforestation, speed up the switch to electric vehicles and encourage investment in renewables [5–7]. Regarding renewables, it must be said that a continuous and ongoing effort is made by Nations in developing and installing more and more renewables based technologies for electric generation. Indeed, as reported in Fig. 1, the renewable share of annual capacity expansion has increased in the last 20 years, starting from 25% in 2001 and reaching an overall of 82% in 2021 [8].

1.1. Oscillating Water Column (OWC) systems and Wells turbine in the wave energy scenario

Unlike other renewable sources, which are currently used on a large scale, the marine energy sector shows a significant resource potential that has not yet been exploited. Indeed, the potential of ocean energy resources can range from 40000 TWh to 130000 TWh per year and depends on the technology involved, as illustrated in Fig. 2 [9,10].

In particular, wave energy technology shows a significant exploitable potential and it is suitable for those areas characterized by advantageous conditions of wave height, wave speed and wavelength. Typically, these physical properties maximize the exploitable power in areas at latitudes within 30 and 60° and in deep water (greater than 40 m). Despite the seasonal variation, waves can be considered a valid energy source, since it is possible to accurately forecast them with the current level of technology. In order to increase the global installed capacity, the European Union has proposed the *European offshore renewable energy strategy* with the aim to reach at least 1 GW of tidal and wave energy by 2030 and 40 GW by 2050 [11]. Obviously, this development must also be

economically feasible, for instance guaranteeing an appropriate levelized cost of energy (LCOE) [12]. According to current estimates, the LCOE for wave energy is between USD 0.30–0.55/kWh, but they are expected to decrease as the technology becomes more and more established. For example, the LCOE of wave energy based technologies is forecast to reach about USD 0.165/kWh by 2030 [13,14].

Among the wide range of technologies, Oscillating Water Column (OWC) devices can be considered the most mature ones for wave energy harvesting [15,16], showing a Technology Readiness Level (TRL) equal to 8 [9]. Basically, OWC systems consist of an *ad hoc* designed chamber, which is semi-submerged in the water, which is still being studied and improved, as demonstrated by several recent works [17–22]. Recently, OWC wave energy converters integrated with floating offshore wind turbines are a promising solution for hybrid offshore renewable energy production [23–25]. The periodic motion of the waves causes an oscillating movement of the water contained in the structure. This effect, in turn, alternately compresses and expands the volume of overlying air, which is conveyed into a duct containing the Power Take-Off (PTO) system. Since the air flow direction alternatively changes, OWC systems

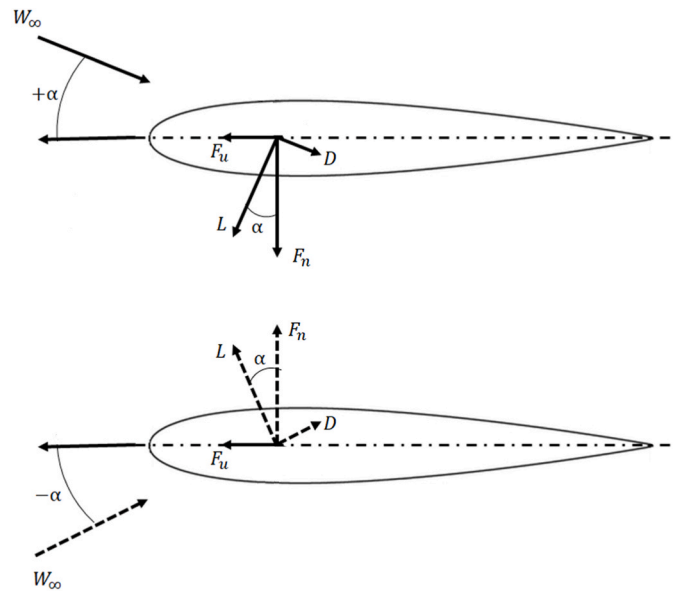


Fig. 3. Forces acting on a typical Wells turbine blade under oscillating flow rate.

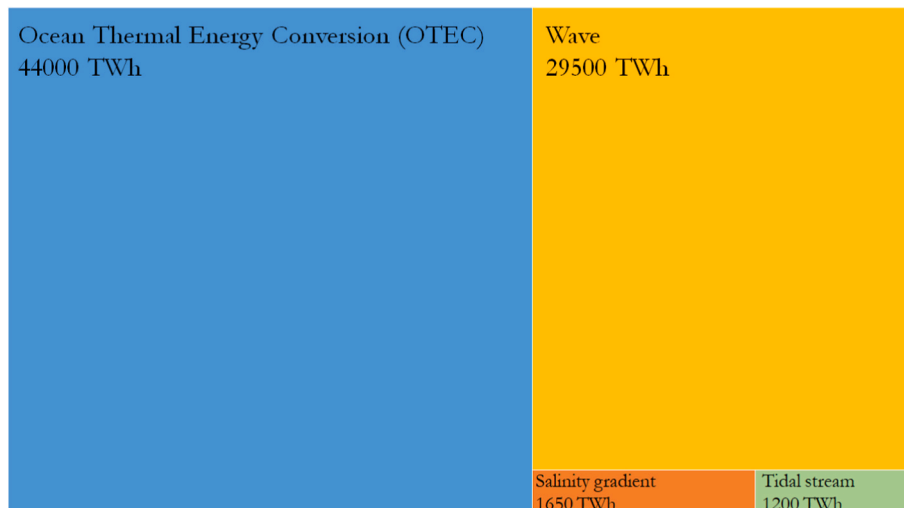


Fig. 2. Ocean energy resource potential.

require self-rectifying machines, for instance Wells turbines [26]. Indeed, the Wells turbine shows its distinctive feature in rotating in the same direction irrespective of the oscillating air flow direction. This can be explained by the operating principle behind the development of this machine, which dates back to 1980's [27]. As depicted in Fig. 3, its blades with symmetrical airfoils, staggered at a 90 deg angle, allow the tangential force to be applied always in the same direction.

As an example of an OWC technology-based power plant, Mutriku wave energy plant, located in the bay of Mutriku (Spain), can be mentioned. The power plant is able to provide a total rated power of about 296 kW thanks to 16 OWC chambers, each of them coupled with a 18.5 kW self-rectifying Wells turbine. As reported in Refs. [28,29], the operation of this kind of plants is not easy, due to the high energy content of the area. Indeed, from the construction (in 2006) to the inauguration (in 2011), the plant suffered severe damages due to strong storms. During its first five years of operation, it supplied over 1.3 GWh to the grid. In 2020, the Mutriku plant produced a cumulative total of 2 GWh [30,31]. Falcão et al. [32] presented a comprehensive review on OWC technology, analyzing all the power plants that have been built since the 2000s. Recently, Monteiro et al. [33] evaluated the possibility of a maritime natural cave for energy production by means of a Wells turbine. Once built, the experimental setup was able to supply electricity to at least 13 houses.

However, the Wells turbine shows a series of drawbacks, such as low aerodynamic efficiency, narrow operating range, poor self-starting characteristics, high axial force coefficient and low tangential force coefficient [34]. For this reason, a significant number of numerical and experimental works have been carried out to improve the performance of Wells turbines. For instance, Gato et al. [35] carried out an experimental campaign on two types of blades: the former with constant thickness and the latter with a variable thickness by keeping unchanged the solidity, the number of blades and chord length. Moreover, it was investigated the beneficial effect of guide vanes to remove flow swirl at the exit. Also Takao et al. [36] conducted a similar analysis. Indeed, they considered a blade with a thickness increasing from the hub to the tip (in details, NACA0015 at hub, NACA0020 at midspan and NACA0025 at tip). From experimental tests, both efficiency and stall operating conditions were improved thanks to this geometry with respect to the conventional one. Torresi et al. [37] performed a detailed CFD analysis on a Wells turbine by comparing numerical results with experimental ones. This analysis showed how the blade tip gap was a key affecting parameter for the overall performance in terms of torque coefficient and efficiency. Among the most recent studies, Abassi et al. [34] numerically investigated the effects of addition of micrometer protrusions similar to shark skin on blades of a Wells turbine. As results, covered blades caused an 18.36% increase in terms of torque and an increase of the turbine efficiency of 2.3%. Kotb et al. [38,39] studied the effect of Gurney flap geometry and the integrated casing groove on the Wells turbine performance. In details, their study outlined how a triangular casing groove in combination with a rectangular Gurney flap allows to increase the average torque coefficient of the machine by 81% with respect to the conventional Wells turbine. Geng et al. [40] carried out an audit and quantification of losses that occur inside the Wells turbine, highlighting how the secondary flow loss coupled together with friction losses present the greatest weight. Ciappi et al. [41,42] proposed wave-to-wire models with an interesting compromise between accuracy and computational costs. Gurnari et al. [43] performed unsteady numerical simulations to study the interaction between waves and a U-shaped OWC breakwater equipped with a Wells turbine, focusing on energy conversion process from wave to the turbine power output. Shaaban et al. [44] numerically investigated the effects of a Venturi duct geometry in order to enhance the Wells turbine performances, reaching up to 9% with the optimized geometry. Alves et al. [45] carried out experimental tests on a Wells turbine with specially designed guide vanes. The presence of the guide vanes was found to increase the peak efficiency by seven percentage points, while reducing (for fixed rotational speed) the damping

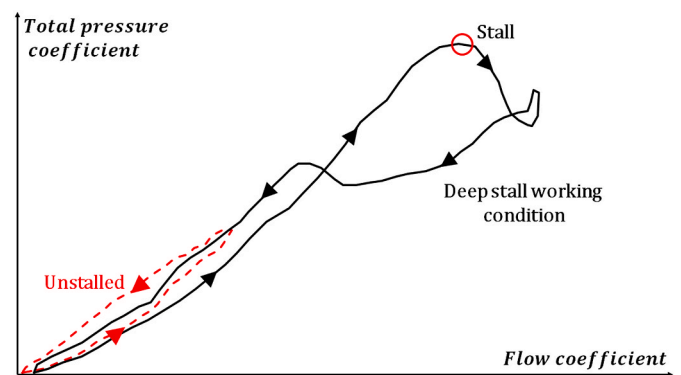


Fig. 4. General behavior of a hysteresis loop under unstalled and deep stall conditions of a Wells turbine (adapted from Ref. [27]).

provided by the turbine. The addition and the design of the guide vanes was investigated also by Mahrooghi et al. [46] by using hybrid artificial neural fuzzy networks. Starzmann and Carolus [47] proposed a novel blade design method based on skewed blades. After numerical and experimental analysis, they found that optimal backward/forward blade skew from hub to tip delayed the onset of stall by increasing the range of unstalled operation with respect to the conventional straight blade design. Kumar et al. [48] proposed a new design of the Wells turbine blade, able to increase the performance range by 22% and the power by 97%, but decreasing the efficiency by 7.7% due to increased pressure drop. This change in performance was due to a solution with a blade characterized by a variable-thickness, a curved radial edge blade and an extended trailing edge.

Although a Wells turbine could reach high efficiencies, its performance is strongly affected by dynamic stall phenomenon, which involves a typical hysteretic behavior, in terms of non-dimensional parameters, during high amplitude flow rate oscillations. Actually, a considerable number of works have been performed with the aim to analyze both experimentally and numerically the hysteresis loop of a Wells turbine during unsteady working conditions. For instance, Paderi et al. [49] and Puddu et al. [50] found out that hysteresis is more evident during outflow and negligible during the inflow period. Setoguchi et al. [51] carried out a numerical investigation to understand the influence of blade thickness, solidity and mounting angle. This analysis found out that the hysteresis loop was less affected by blade thickness than the other two parameters. Thakker and Abdulhadi [52,53] performed an experimental and a numerical campaign on a Wells turbine under unsteady inlet flow conditions by focusing on the effects of blade profile and solidity. Kim et al. [54] focused on the tip clearance and the hub-to-tip ratio, showing how the former (specifically its increase) has a greater effect on the hysteresis loop than the latter. Licheri et al. [55,56] presented a detailed experimental campaign with the aim to test their proposed control strategy based on the turbine rotational speed in order to avoid stall conditions and allow the machine to work as close as possible to the maximum efficiency point.

However, all these works even if were focused on hysteresis phenomenon, they did not considered inlet flow conditions capable to determine the so-called deep stall. As depicted in Fig. 4, when the machine experiences strong variations of flow rate, the stall occurs with a clockwise hysteresis loop. Indeed, Fig. 4 shows typical performance curves of a Wells turbine in terms of non-dimensional parameters, which will be discussed in detail in the next sections (i.e., the torque coefficient, T^* , vs. the flow coefficient, U^*). This phenomenon is due to the flow separation, close to the tip, on the blade suction side, as evidenced by experiments performed by Setoguchi et al. [57]. Moreover, Ghisu et al. [58] argued that the cause of the hysteresis loop was related to the compressibility effect in the OWC system. M'zoughi et al. [59] proposed a rotational speed control based on artificial neural network in order to

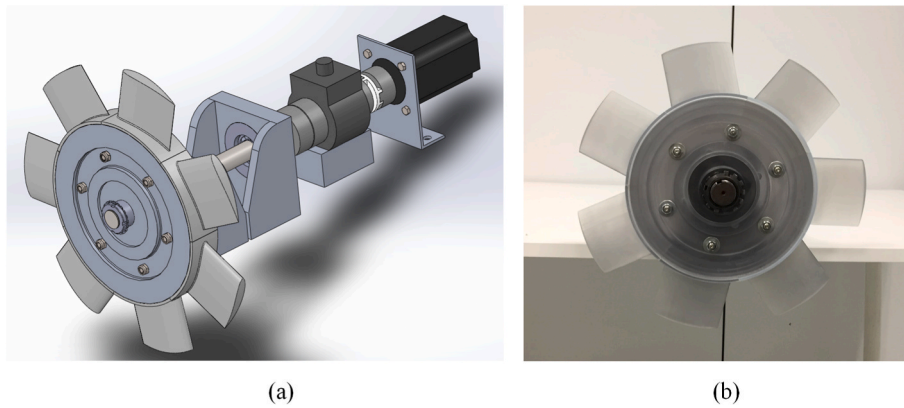


Fig. 5. 3D model of the designed Wells turbine (a); View of the 3D-manufactured model of the Wells turbine (b).

avoid stall operating conditions of a Wells turbine installed in a OWC.

Actually, during stall the Wells turbine experiences evident torque fluctuations, which overlay on the typical hysteresis loop, mainly during flow deceleration. The amplitudes of these fluctuations are damped as the flow rate decreases toward reattachment. Often these fluctuations are not evident because hysteresis loops are usually provided with phase-averaged data, which can significantly smoothen or even conceal them. Indeed, it is difficult to find in the literature high frequency torque measurements able to show these fluctuations. To the authors' knowledge, the experimental investigation of Wells turbines in dynamic deep stall conditions has not been fully addressed and deepened. Indeed, only Kinoue et al. [60] in 2004 showed experimental performance curves of a Wells turbine under deep stall conditions. They found out that the experimental torque coefficient fluctuates greatly after the stall condition, with the number of peaks varying from two to three, without going into too much depth and analyzing the phenomenon with different wave periods. Moreover, thanks to their numerical studies, they sustained that the mechanism of the clockwise loop under deep stall condition is related to the dynamic stall of an airfoil and it can be associated with the flow separation on the blade suction side near the tip. Starzmann et al. [61] investigated the effects of solidity and hub-tip ration on the Wells turbine performance. They also introduced the hysteresis loop coefficient, h (i.e., the ratio between the pressure coefficient at the maximum power and that in correspondence of flow reattachment). Three rotors were compared in terms of experimental hysteresis loops, which however showed few experimental points after the stall. Furthermore, no differences are shown between the accelerating and decelerating phases. In addition, the same authors argued that the obtained results did not necessarily hold true for scaled up turbines since stall and hysteresis are associated with the complex stability phenomena. Puddu et al. [62] carried out an experimental campaign to characterize a Wells turbine under unsteady and bi-directional airflow. Most of the tests were under unstalled conditions and only during one test a stall condition was reported. Although the torque coefficient curve showed fluctuations, this phenomenon was not explored. Afterwards Hu et al. [63] numerically investigated a high-solidity Wells turbine under both steady and unsteady conditions by solving URANS equations. However, regarding unsteady conditions, they analyzed different wave periods only in the unstalled conditions without exploring deep stall zones. Moreover, Ghisu et al. [64] numerically investigated with unsteady CFD simulations the hysteresis for unstalled and stalled operating conditions by evaluating the influence of the temporal discretization. The numerical results for the stall conditions in terms of torque coefficient vs. the flow rate coefficient reported strong oscillations of the torque coefficient only after the stall, restricted to a range of flow coefficients between stall and reattachment. However, it is sustained that no differences are evident between the torque coefficients in deceleration and acceleration after the flow reattaches, despite small oscillations are visible.

Finally, Geng et al. [65,66] recently performed a loss audit by means of a CFD analysis to better understand the aerodynamic loss mechanisms in the Wells turbine during stall process. As a result, they proposed an improved vortex identification method that takes into account coherent structures and vortex core trajectories to highlight the relation between vortex interactions and stall mechanism. However the investigated machine is equipped with guide vanes and the numerical investigation is performed by means of URANS approach under steady inlet flow conditions; hence, the hysteretic behavior of the machine during stall is not evaluated.

Then, the present work aims to fill the knowledge gap on the behavior of the Wells turbine under dynamic stall conditions. With the aim to better investigate the torque oscillations triggered by the stall, a 3D-printed monoplane Wells turbine has been tested at the open wind tunnel of the Polytechnic University of Bari, Italy (<https://research.polib.a.it/laboratories/we-wt-lab>). The novel contribution of this work consists in proposing a comprehensive experimental analysis of the machine working under unsteady cyclic inlet flow conditions in order to highlight how the stall triggers this phenomenon. Moreover, the analysis is mainly focused on the effects of the main parameters of the oscillating inlet flow conditions on the performance of the machine (mean flow rate, amplitude and period of oscillation). These unsteady cyclic inlet flow conditions have been generated by modifying the controlling parameters of the inverter, which drives the blower (i.e. the mean frequency, \bar{f} , the frequency amplitude of the inverter, Δf , and the period, T). Hence, detecting these torque oscillations, triggered once the stall occurs, can be relevant in the turbine design phase to enhance the structural strength of the turbine.

In this framework, the work initially gives an overview on renewable energy mix, focusing on the current blue energy scenario and its related technologies. In details, OWC systems and Wells turbine are particularly investigated (section 1). Then, section 2 describes the Wells turbine designed and tested at the lab of the Polytechnic University of Bari, which is described in section 3. Afterwards, section 4 and 5 illustrate the experimental campaign voted to characterize the turbine under steady and dynamic stall flow conditions, respectively. Finally section 6 ends up the work with a sum up and the discussion of the results.

2. The Wells turbine

Fig. 5 shows a view of the 3D printed Wells turbine under investigation, whose design parameters (i.e., turbine solidity, hub-to-tip ratio and blade airfoil) have been chosen in order to design a prototype suitable for a 1:10 scaled model of a REWEC (Resonant Wave Energy Converter) breakwater, located in Reggio Calabria, Italy [67]. As previously mentioned, the turbine rotor has been created by means of a 3D printer (named Stratasys Object30 Pro) and it is made of VeroClear material, a transparent PolyJet photopolymer.

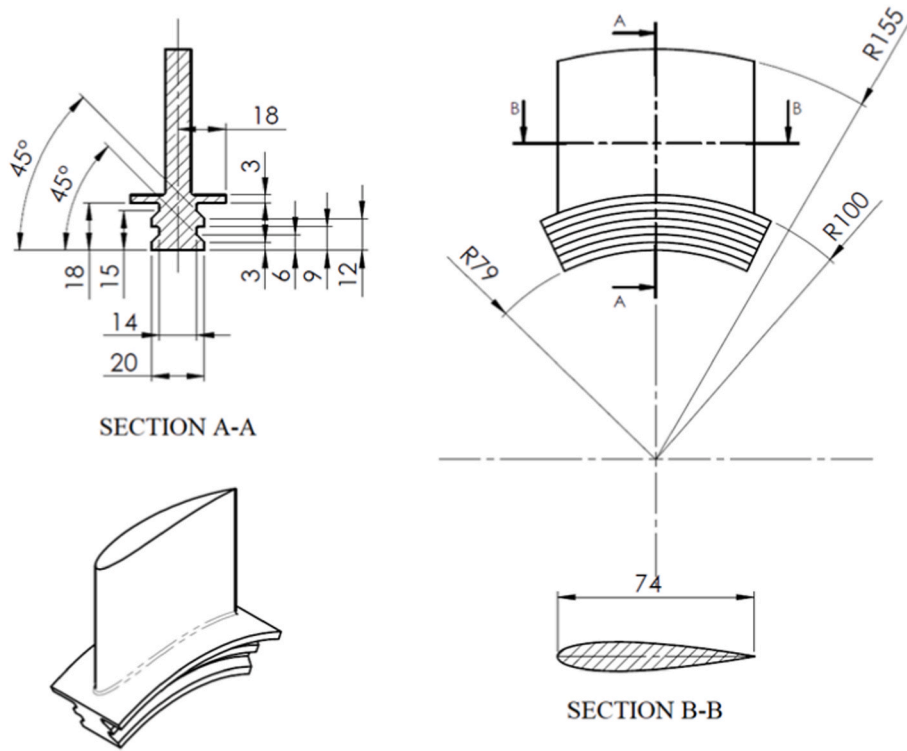


Fig. 6. Technical drawing of the blade of the Wells turbine under investigation.

Fig. 6 represents the technical drawing of the designed blade, characterized by a constant chord ($c = 74$ mm) and a NACA0015 profile. In

details, hub and tip radii are 100 mm and 155 mm, respectively. Finally, the rotor is constituted by 7 blades ($N_b = 7$). Hence, the prototype shows a solidity $s = 0.6466$, which is defined according to equation (1).

$$s = \frac{N_b c}{2\pi R_{mid}} \tag{1}$$

where R_{mid} is the mid span radius, defined as follows:

$$R_{mid} = \frac{(1 + h)R_{tip}}{2} \tag{2}$$

with $h = R_{hub}/R_{tip}$ the hub-to-tip ratio.

Performance of a Wells turbine can be evaluated by means of non-dimensional parameters. These parameters are the flow coefficient, U^* , the stagnation pressure drop coefficient, Δp^* , the torque coefficient, T^* , and the efficiency, η . Specifically, the flow coefficient, U^* , is defined as the ratio between the bulk axial velocity of the air, evaluated upstream the turbine, and the peripheral velocity evaluated at the blade tip (see equation (3)).

$$U^* = \frac{V}{\omega R_{tip}} \tag{3}$$

Equation (4) defines the stagnation pressure drop coefficient, Δp^* , as follows:

$$\Delta p^* = \frac{\Delta p_0}{\rho_{air} \omega^2 R_{tip}^2} \tag{4}$$

with ρ_{air} and Δp_0 the air density and the stagnation pressure drop, respectively.

The torque coefficient, T^* , is determined by equation (5):

$$T^* = \frac{T_t}{\rho_{air} \omega^2 R_{tip}^5} \tag{5}$$

Where T_t is the aerodynamic turbine torque, i.e. the torque applied by the flow to the blade. As explained in previous works [68,69], this



(a)



(b)

Fig. 7. Views of the test rig (GaVe lab at the Polytechnic University of Bari, Italy).

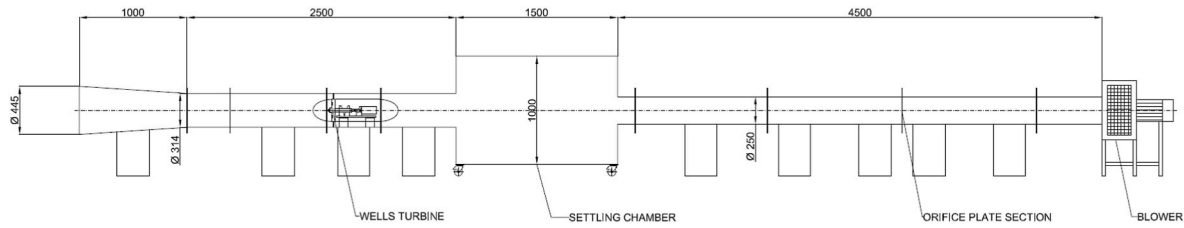


Fig. 8. Schematic of the test rig (GaVe lab at the Polytechnic University of Bari, Italy).

torque is different from that measured by means of the torque meter, $T_{Torque\ meter}$, because of the aerodynamic windage and mechanical frictions. From an experimental point of view, it is possible to assess these two contributions. Precisely, the turbine is motored by an electric motor without air flow in a wind tunnel, which will be described in the next section. The absence of the air flow is achieved by keeping the blower off. In this way, the torque meter is able to measure $T_{Torque\ meter}^{no\ flow}$, which include not only windage and friction losses, but also the drag of the blades. Indeed, without air flow (i.e., $V = 0\ m/s$), the angle of attack of the flow is equal to 0 deg. The torque related to the drag, $T_t^{no\ flow}$, was derived from 3D CFD simulations performed in previous works by Torresi et al. [37]. Hence, the aerodynamic turbine torque, T_t , can be computed as follows:

$$T_t = -T_{Torque\ meter} + T_{Torque\ meter}^{no\ flow} - T_t^{no\ flow} \tag{6}$$

Once computed T_t , the efficiency of the turbine, η , can be evaluated by means of equation (7), where P_p is the available pneumatic power, $P_p = Q\Delta p_0$.

$$\eta = \frac{\omega T_t}{P_p} \tag{7}$$

3. The test rig

Fig. 7 shows the view of the test rig employed in the experimental campaign, whereas Fig. 8 shows a technical schematic of the test rig with all the main geometric information.

Fundamentally, it consists of an open circuit wind tunnel (of the suction type) and is located in the GaVe lab at the Polytechnic University of Bari, Italy. The Wells turbine is installed inside the first duct (3.5 m long), which is constituted of a first convergent duct (with a length $L = 1\ m$, inlet and outlet diameters $D_{IN} = 445\ mm$, $D_{OUT} = 314\ mm$, respectively). Then, a settling chamber (1.5 m long, 1.0 m wide and 1.0 m high) cancels tangential velocity components thanks to an inner honeycomb structure. This chamber is connected to the blower by means of a 4.5 m long duct, where the flow rate measurements are performed according to the ISO 5147-1 standard. Indeed, this part is equipped with a section where it is possible to install different orifice plates chosen as pressure differential devices. Each plate is characterized by a diameter ratio, β , (defined as the ratio between the orifice diameter and the inner diameter of the duct). Precisely, $\beta = 0.2, 0.3, 0.4, 0.5, 0.6$ and 0.75 are used in order to reduce measurement uncertainty for different flow rates. The relative pressure upstream the orifice is measured by means of a Honeywell 163PC01D36 amplified pressure transducer (pressure range of $\pm 5''\ H_2O$ – accuracy $\pm 2\%$). In addition, the differential pressure value across the orifice is measured by means of a Honeywell 164PC01D76 amplified pressure transducer. This device is characterized by a pressure range of $0\div 5''\ H_2O$ and accuracy $\pm 2\%$. A squirrel cage blower (model A0 112M-4 by ELPROM) is installed at the end of the wind tunnel. The blower has the key role to generate the air flow. It is driven by an AC electric motor (2 poles, nominal power equal to 4.1 kW at 1430 rpm), which in turn is powered by a vector control drive, model V1000 by Omron (nominal power of 5.5 kW). Changing the frequency of the inverter is then possible to vary the flow rate. Regarding the

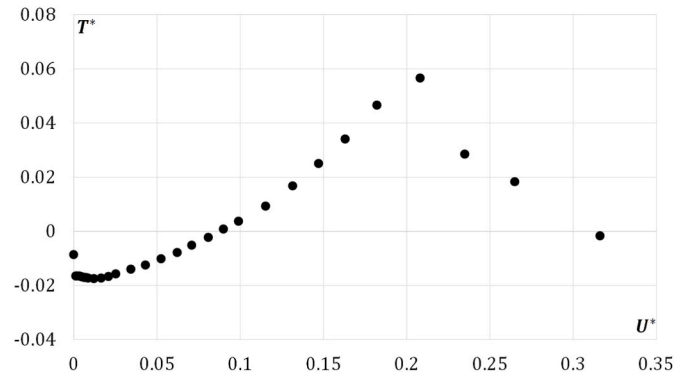


Fig. 9. Steady state experimental curve in terms of torque coefficient T^* vs. flow coefficient U^* .

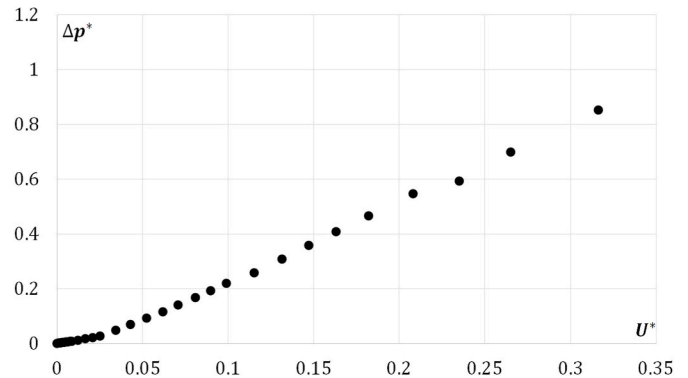


Fig. 10. Steady state experimental curve in terms of stagnation pressure drop Δp^* vs. flow coefficient U^* .

equipment useful to measure the performances of the Wells turbine, a second Honeywell 163PC01D36 amplified pressure transducer is used to measure the stagnation pressure drop across the turbine. In order to measure the pressure drop, one side of the transducer is connected to a pressure tap in the settling chamber, whereas the other side is open to the atmosphere. Moreover, a P-Series SanyoDenky Servo Motor with an embedded encoder is coupled to the turbine to be used as an electric generator. In addition, the torque is measured by the torquemeter T22/5NM by HBM ($T_{max} = 5\ Nm$, accuracy class 0.5). Finally, an in-house Supervisory Control and Data Acquisition (SCADA) system developed in the NI LabVIEW® environment manages and controls the entire rig during tests.

4. Experimental characterization - steady working conditions

As a first step, the Wells turbine has been tested under steady state conditions at 1750 rpm. The performance of the Wells turbine under steady state conditions are reported in Figs. 9–11. Each flow rate is generated by varying the frequency of the control vector drive (hence,

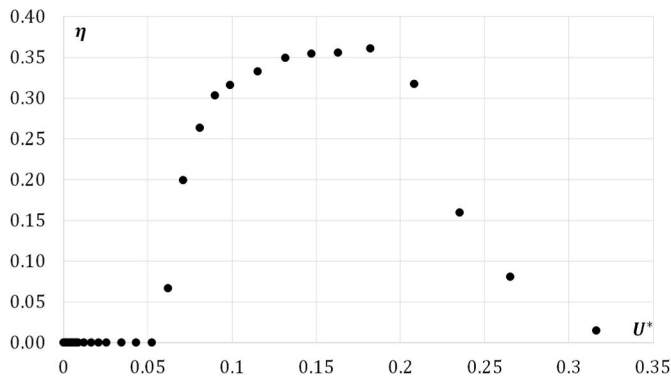


Fig. 11. Steady state experimental curve in terms of stagnation pressure drop η vs. flow coefficient U^* .

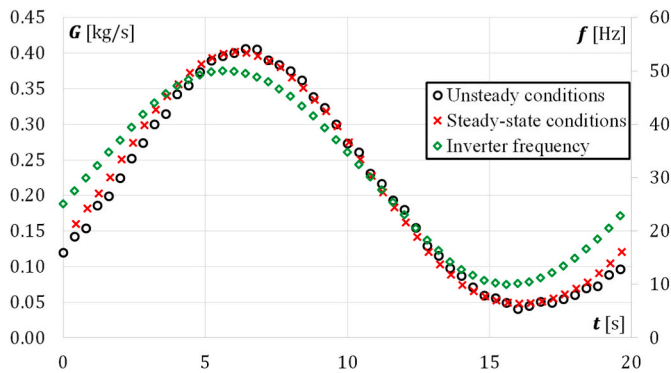


Fig. 12. Comparison of the mass flow rates during steady and unsteady experimental tests.

the velocity of the blower) up to 60 Hz with steps of 5 Hz. In such a way, it was possible to explore the entire operating range of the turbine, as well as to measure the different flow rates with the orifice, characterized by the best β to give the smallest uncertainty on the dimensionless parameter U^* . In details, these figures show the experimental T^* , Δp^* , and η , vs. U^* , respectively.

Looking at Fig. 9, it is possible to notice how the turbine is not self-starting. Indeed, the torque coefficient becomes positive only after a determined value of the flow coefficient, i.e. $U^* = 0.07$. Below this value, the machine needs to be driven by the electric motor. As the flow rate, and therefore the flow coefficient, increases, the torque coefficient also increases up to a value close to $U^* = 0.21$ and then drops suddenly due to stall. In this condition, the flow around the blade profile separates at the so-called static stall angle. The significant performance drop of the turbine is due to higher angles of attack than the stall limit [70].

Moreover, Fig. 10 highlights the intrinsic characteristic of this type of machine, regarding the stagnation pressure drop. Indeed, the Wells turbine shows a linear correlation of Δp^* vs. U^* . Finally, the efficiency curve in Fig. 11, shows null values for U^* up to 0.07, then increases as the flow rate increases up to its maximum $\eta = 36.1\%$. After that, stall occurs and the efficiency significantly drops for higher flow rates as the torque coefficient does. For the sake of clarity, the null values of the efficiency are due to the fact that the turbine is driven by the electric motor for those flow conditions.

5. Experimental campaign - unsteady working conditions

As mentioned in the introduction, several tests have been carried out on the Wells turbine under unsteady flow conditions, with the aim to focus on the effects of both the amplitude and the frequency of the flow rate oscillations on the hysteresis loops when either unstalled or deep

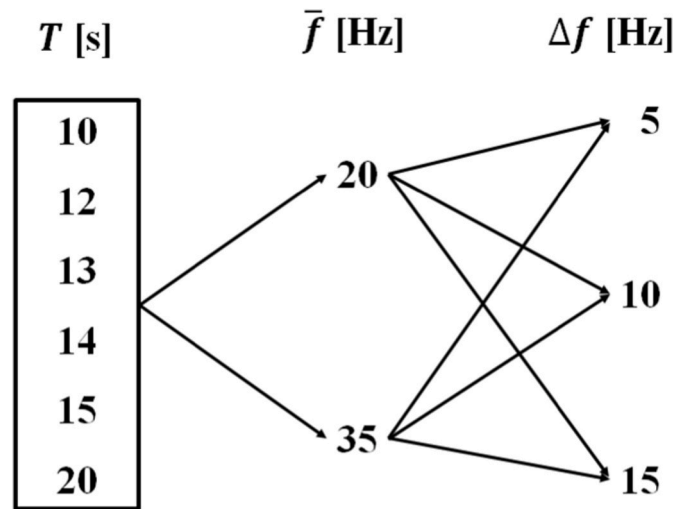


Fig. 13. Design of experiment employed in the experimental campaign.

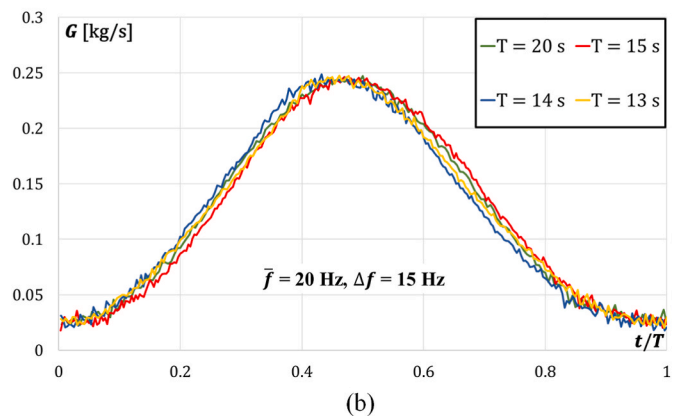
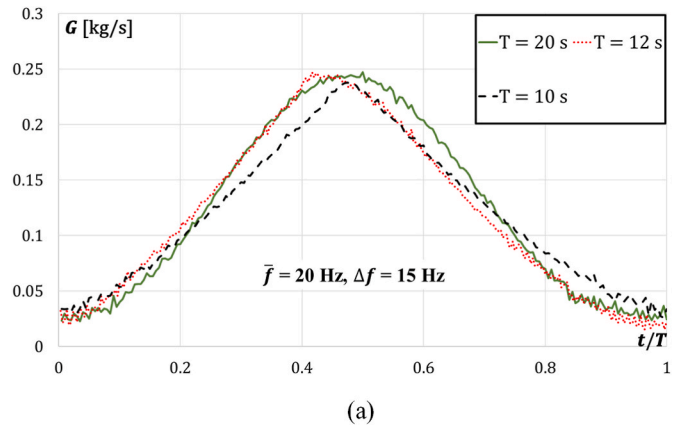


Fig. 14. Comparison of the mass flow rate time evolutions for different periods of the sinusoidal frequency signal sent to the blower. Comparison between $T = 10, 12, 20$ s (a), and $T = 13, 14, 15, 20$ s (b) (case $\bar{f} = 20$ Hz, $\Delta f = 15$ Hz).

stall conditions are reached. Actually, in order to replicate flow oscillations such as in the real working conditions of OWC systems, the blower has been driven cyclically with a frequency, f , which changes sinusoidally according to equation (8), for 30 cycles. Indeed, this sinusoidal changing of the frequency involves the same oscillating variation of the flow rate. In addition, the turbine has been tested at 1750 rpm.

$$f(t) = \bar{f} + \Delta f \sin(2\pi t / T) \tag{8}$$

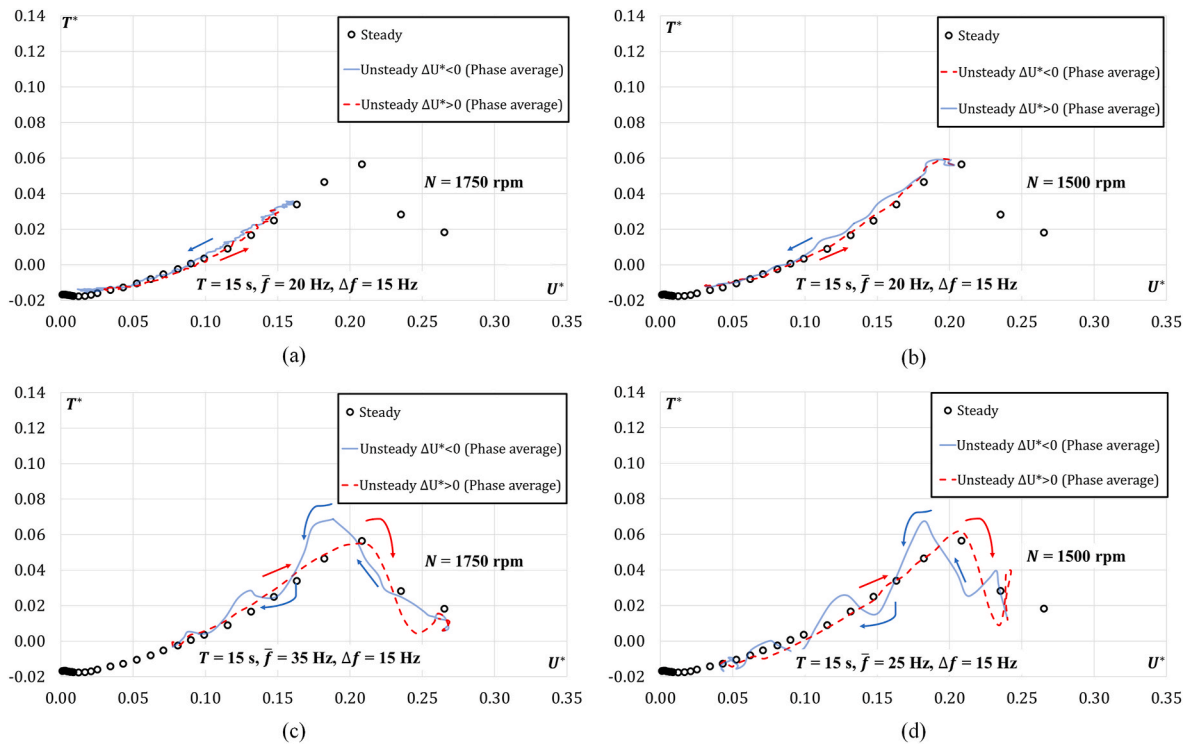


Fig. 15. Torque coefficient T^* vs flow coefficient U^* under unstalled conditions at $N = 1750$ rpm (a) and $N = 1500$ rpm (b) (case with $T = 15$ Hz, $\bar{f} = 20$ Hz, $\Delta f = 15$ Hz); and dynamic stall conditions at $N = 1750$ rpm (c) and $N = 1500$ rpm (d).

Fig. 12 represents the phase-averaged mass flow rates, G , and the inverter frequency, f , measured during unsteady tests over a period of 20 s, evidencing a delay in the mass flow rate variation. In order to verify that there is only a delay during steady state test, a third curve is plotted, which is obtained by considering the mass flow rate values computed at each frequency and then shifting it in order to superpose this curve to the averaged unsteady mass flow rate. This aspect confirms the reliability of mass flow rate measurements even during unsteady working conditions.

The design of experiments (DOE) carried out in this work is represented in the scheme of Fig. 13. Different values of periods, T , have been considered (i.e., $T = 10, 12, 13, 14, 15$ and 20 s). The lower limit (i.e., $T = 10$ s) is due to technical limitation of the test rig which does not allow to perform tests with lower periods, as explained in the following Fig. 14. In order to evaluate both hysteresis loops under unstalled and deep stall conditions, two mean frequency values, \bar{f} , of the inverter have been selected (i.e., $\bar{f} = 20$ and 35 Hz). Then, for test identified by each set of T and \bar{f} , two frequency amplitude values, Δf , have been considered (i.e., $\Delta f = 10$ and 15 Hz). Definitely, 36 tests have been carried out. In order to summarize the results, not all the cases will be shown but only the most interesting in terms of specific working conditions.

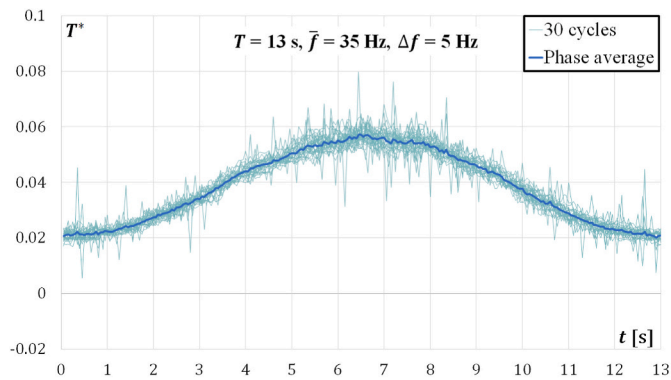
The reason behind the choice of different periods is related to the objective of understanding what are the operating limits of the machine. Looking at Fig. 14(a) and (b), it is possible to evaluate the time evolution of the mass flow rate, G , for different periods. For the sake of brevity, the comparison has been carried out by keeping constant $\bar{f} = 20$ Hz and $\Delta f = 15$ Hz, and changing the period, T . In Fig. 14(a), the lowest periods ($T = 10$ and 12 s) have been compared with the highest one ($T = 20$ s), in order to better highlight the significant difference between their time evolutions. Indeed, the flow rates acquired at $T = 12$ s and 10 s lose the typical sinusoidal trend, that is expected during normal operating conditions. This can be caused by the delay between the induced flow rate crossing the turbine and the variation of the blower rotational speed. This issue does not happen for the cases at $T = 13, 14, 15$ and 20 s, as visible in Fig. 14(b). Then, the period $T = 13$ s has been selected as the minimum period above which the machine is crossed by a coherent mass

flow rate.

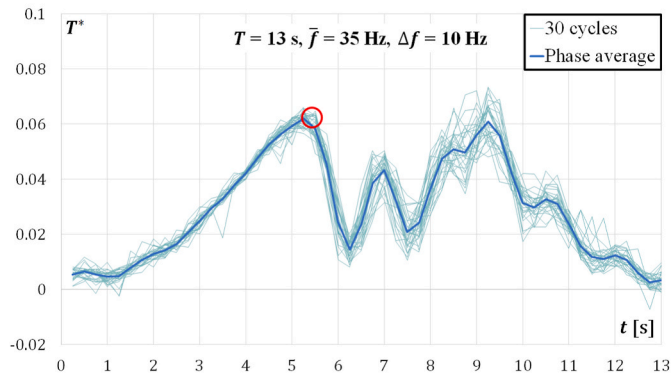
5.1. Effects of the mean frequency of the inverter \bar{f}

Fig. 15 shows the clear difference between hysteresis loops under unstalled and deep stall conditions. In both the cases, the unsteady curves are compared with respect to the steady state torque coefficient curve. In detail, Fig. 15(a) shows the typical cycle without stall (case at $T = 15$ s, $\bar{f} = 20$ Hz, $\Delta f = 15$ Hz). It is possible to notice how the unsteady curve is constituted of the upward branch (the dashed red line) and the downward branch (in blue), which follow the steady state curve. Moreover, this curve has been obtained by means a phase averaging over the 30 cycles and no hysteresis loop occurs. The unsteady curve in Fig. 15(c) has been obtained by changing only the inverter mean frequency $\bar{f} = 35$ Hz, keeping unchanged the period and the frequency amplitude with respect to the case of Fig. 15(a). In this way, the turbine works with greater mass flow rate, reaching and passing the stall condition. This results in a counter-clockwise hysteresis loop, which is due to the different turbine behavior during the acceleration (the dashed red line) and deceleration of the flow (in blue), in accordance with the studies by Kinoue et al., which sustained that it can be associated with the separation on the blade suction side near the hub [60]. Particular attention must be paid on what happens once dynamic stall occurs. Indeed, marked damped oscillations emerge and persist during the deceleration phase, postponing the flow reattachment. The amplitude of these oscillations decreases as the flow rate decreases during the clockwise hysteresis loop. As a result, the machine shows unstable torque coefficients during deceleration phase.

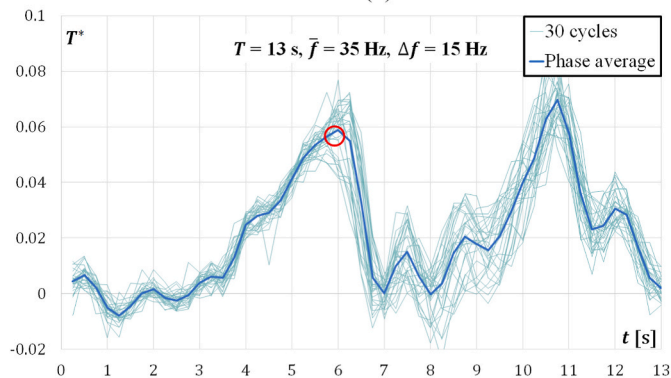
In order to highlight how the stall triggers this phenomenon, an additional test was carried out at lower rotational speed (i.e., $N = 1500$ rpm). This allowed to test the machine under unstalled conditions with flow rate coefficients close to the stall condition, without exceeding it. Indeed, looking at Fig. 15(b), it is possible to notice how the Wells turbine shows the typical hysteresis loop following the steady state points without torque oscillations. Then, the turbine is well controlled



(a)



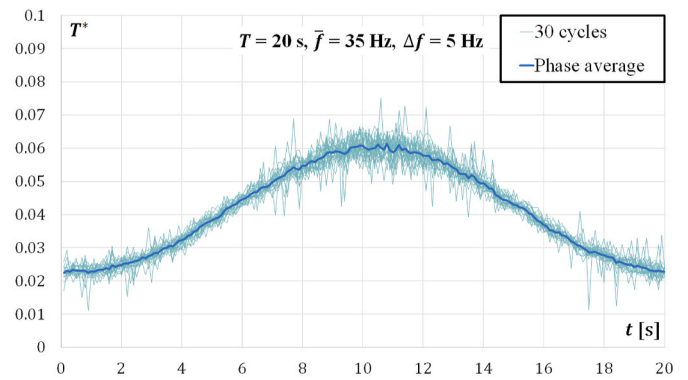
(b)



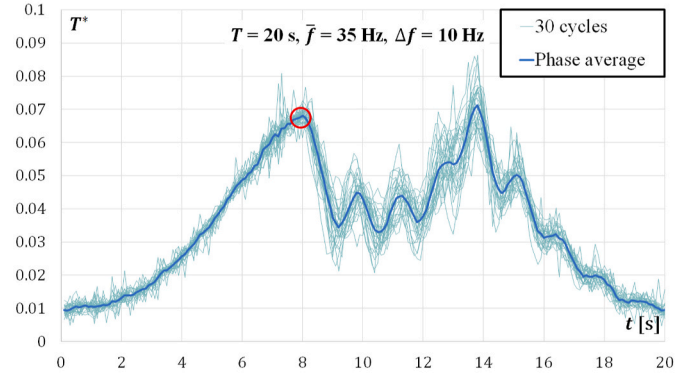
(c)

Fig. 16. Effects of the frequency amplitude, Δf , on the time evolution of the torque coefficient (case with $T = 13$ s, $\bar{f} = 35$ Hz and $\Delta f = 5$ Hz (a), $\Delta f = 10$ Hz (b), $\Delta f = 15$ Hz (c)).

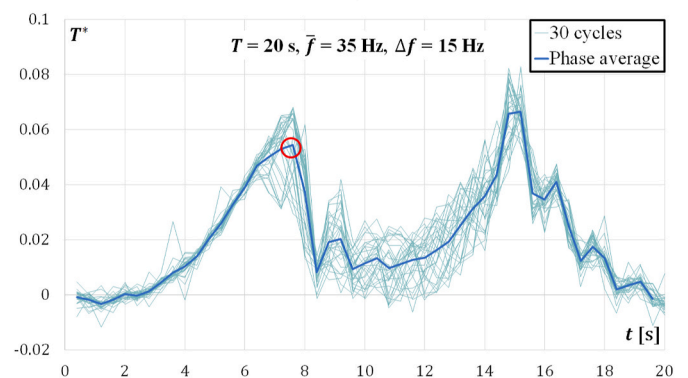
during the cyclic operating conditions. The deep stall condition at 1500 rpm is reported in Fig. 15(d), where it is possible to notice torque coefficient fluctuations as seen in the previous Fig. 15(c). This highlights that the passing of the stall condition triggers this phenomenon. The presence of these fluctuations are also reported in the aforementioned study by Kinoue et al. (see Fig. 6 in Ref. [60]), which sustained that the hysteresis loop under deep stall condition can be associated with the separation on the blade suction side near the tip. Moreover, according to the recent numerical investigations by Geng et al., the stall condition is characterized by loss sources related to kinetic energy and mixing losses. In details, as the leading-edge vortices expand toward the blade tip, the intensified leading-edge vortex interacts with the casing suction-side corner vortex and accelerates the dissipation of the tip-leakage vortices [66].



(a)



(b)



(c)

Fig. 17. Effects of the frequency amplitude, Δf , on the time evolution of the torque coefficient (case with $T = 20$ s, $\bar{f} = 35$ Hz and $\Delta f = 5$ Hz (a), $\Delta f = 10$ Hz (b), $\Delta f = 15$ Hz (c)).

5.2. Effects of the inverter frequency amplitude Δf

With the aim to focus on the impact of the inverter frequency amplitude, Δf , on the turbine performance, two test sets have been selected. For the sake of clarity, the two extreme cases have been selected, i.e., the cases with periods $T = 13$ s and 20 s. Specifically, for each period the comparison has been carried out by keeping constant the mean frequency $\bar{f} = 35$ Hz, but changing the frequency amplitude (i.e., $\Delta f = 5, 10$ and 15 Hz). In details, Figs. 16 and 17 show the comparison between the time evolution over the period of the torque coefficient at different Δf for $T = 13$ s and 20 s, respectively. Moreover, each figure shows both T^* curves acquired over 30 cycles and the corresponding phase-averaged values.

Specifically, Fig. 16(a) shows the less stressful working condition with $\Delta f = 5$ Hz, highlighted by the sinusoidal trend of T^* . Indeed, the

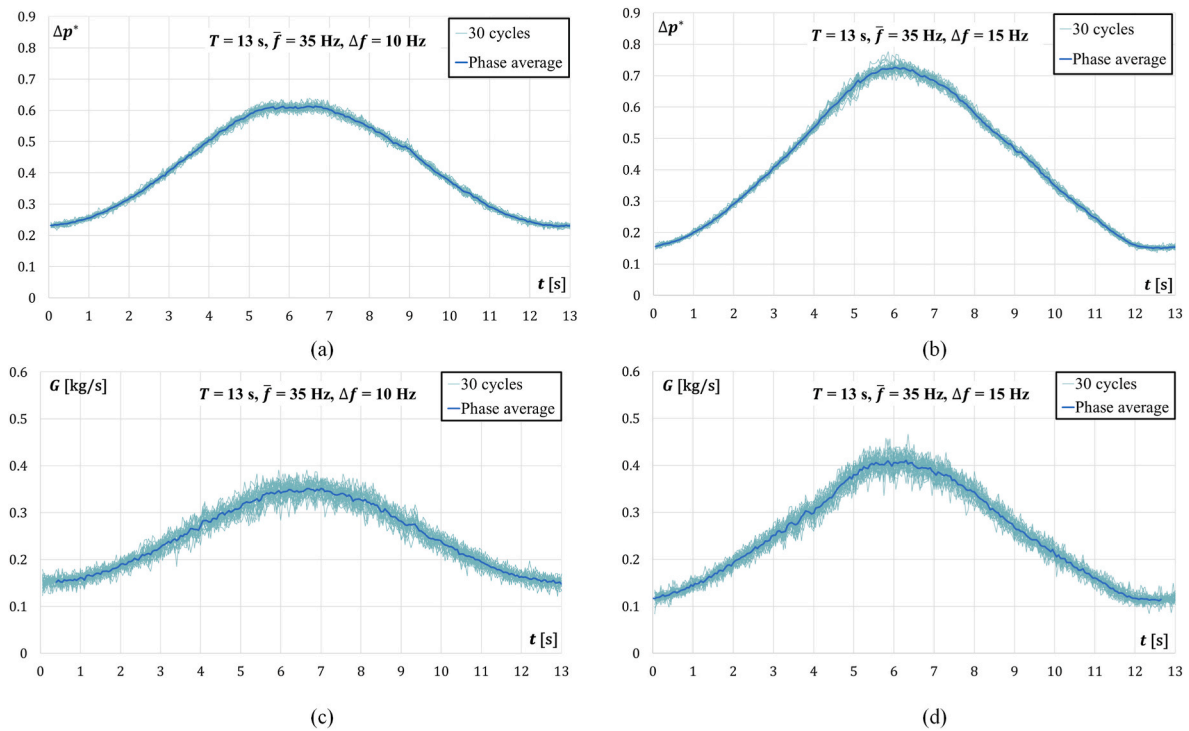


Fig. 18. Phase averaged of the stagnation pressure drop coefficient in no stall condition (a) and dynamic stall condition (b); Phase averaged of the mass flow rate in no stall condition (c) and dynamic stall condition (d) (case with $T = 13$ s).

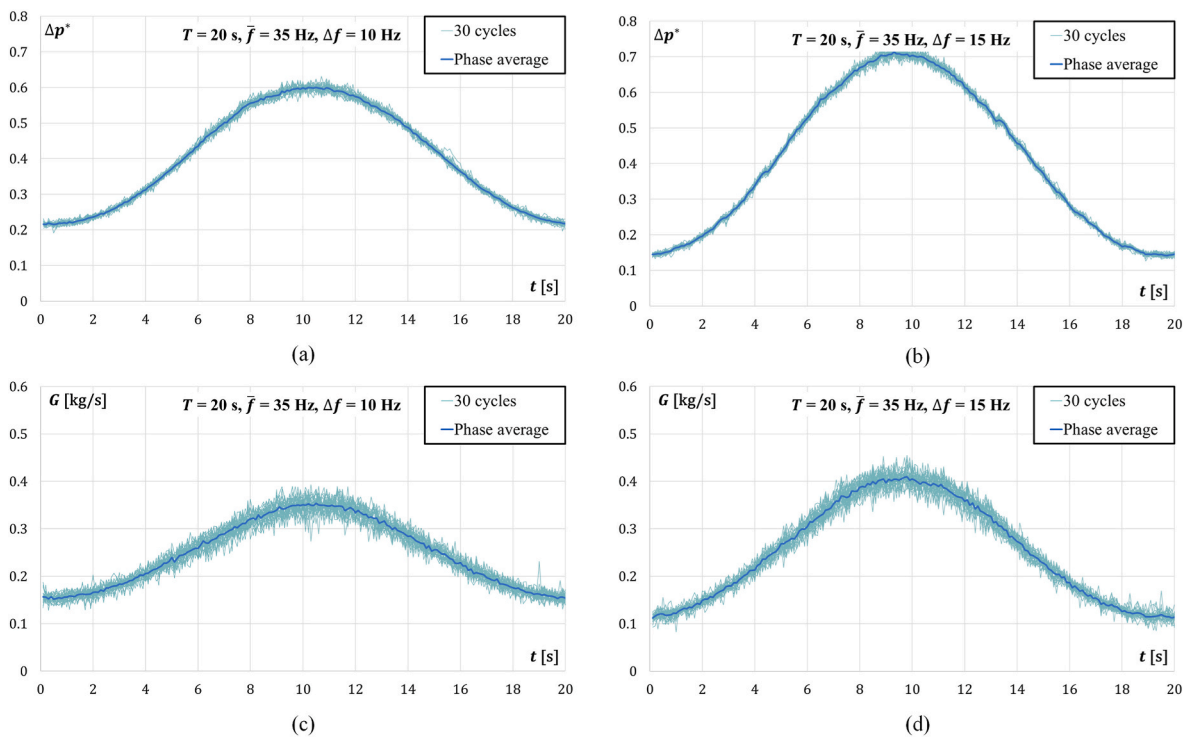


Fig. 19. Phase averaged of the stagnation pressure drop coefficient in no stall condition (a) and dynamic stall condition (b); Phase averaged of the mass flow rate in no stall condition (c) and dynamic stall condition (d) (case with $T = 20$ s).

frequency amplitude is not large enough to induce dynamic stall, as it occurs in Fig. 16(b) and (c). These two figures highlight the effect of the stall on the torque coefficient of the turbine. At the beginning, T^* grows regularly up to the stall condition, emphasized with the red circle, which corresponds to the aforementioned $U^* = 0.21$. After the stall, the

investigated Wells turbine experiences a drastic reduction of the torque coefficient of about 90%. Then, T^* starts to show oscillations which are damped up to the end of the period, hence the cycle begins again. The same considerations can be done looking at Fig. 17, related to $T = 20$ s. Nevertheless, these torque fluctuations are due neither to fluctua-

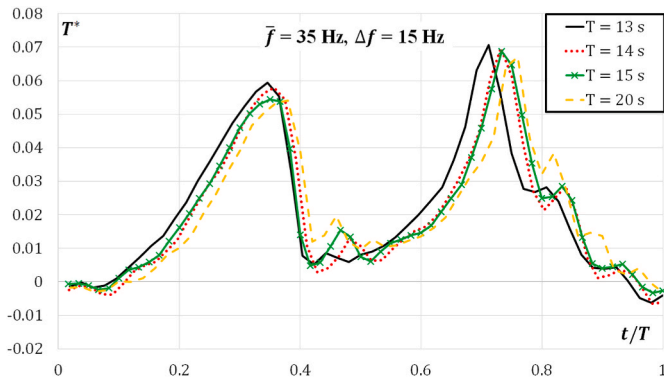


Fig. 20. Effects of the period, T , on the time evolution of the torque coefficient (case with $\bar{f} = 35$ Hz and $\Delta f = 15$ Hz).

tions of the mass flow rate nor of the pressure drop coefficient. This is confirmed by looking at Figs. 18 and 19. Each figure compares the effects of the frequency amplitude variation (Δf from 10 Hz to 15 Hz) on the pressure drop and the flow rate, by keeping constant the mean frequency ($\bar{f} = 35$ Hz) and the period ($T = 13$ s in Fig. 18 and $T = 20$ s in Fig. 19). In both cases, phase-averaged Δp^* curves show a regular and sinusoidal behavior without abnormal fluctuations (see Fig. 18(a) and (b), Fig. 19(a) and (b)). The same considerations can be also applied to the mass flow rate (see Fig. 18(c) and (d), Fig. 19(c) and (d)). For these reasons, they cannot be the cause of the fluctuations present in T^* unsteady curves.

5.3. Effects of the period T

Fig. 20 focuses on the effect of the period, T , on the time evolution of the torque coefficient, T^* . Since different periods are analyzed, the comparison has been carried out by normalizing the time over the period, t/T . Also in this case, the comparison has been carried out by keeping constant $\bar{f} = 35$ Hz and $\Delta f = 15$ Hz. Indeed, it is possible to note

how the accelerating phase is not affected by any fluctuation up to the stall condition for each period. Indeed, the four sections relating to the unstalled conditions overlaps. Then, during the decelerating phase all the T^* curves are characterized by dynamic stall, highlighted by the drastic reduction of the torque coefficient, followed by fluctuations.

A confirmation of these effects can be verified by looking at Fig. 21, where four phase-averaged hysteresis loops under dynamic stall conditions can be compared. Specifically, the comparison regards the more stressful condition, i.e. $\bar{f} = 35$ Hz, $\Delta f = 15$ Hz with all the periods under investigation. In all the four cases, the decelerating phase is characterized by strong torque fluctuations triggered once the stall occurs.

As a result, the machine shows unstable torque coefficients during deceleration phase. The presence of these fluctuations are also reported also in the aforementioned study by Kinoue et al. (see Fig. 6 in Ref. [60]), which sustained that the hysteresis loop under deep stall condition can be associated with the separation on the blade suction side near the tip. Moreover, looking at Fig. 21, the case corresponding to $T = 20$ s shows a greater number of peaks (4) than those related to the other cases (3). As reported also by Kinoue et al. [60], the mechanism behind the clockwise loop can be explained by the concept of the dynamic stall on an airfoil (i.e., the flow separates and reattaches with the time delay for the unsteady flow case, as reported also in Refs. [71,72]). Then, the greater number of peaks can be associated to the greater period in which a single cycle has to be completed. Moreover, according to the recent numerical investigations by Geng et al., the stall condition is characterized by loss sources related to the kinetic energy and mixing losses. In details, as the leading-edge vortices expand toward the blade tip, the intensified leading-edge vortex interacts with the casing suction-side corner vortex and accelerates the dissipation of the tip-leakage vortices [66]. This work also takes as a reference the same 1:10 scaled model of the aforementioned REWEC (Resonant Wave Energy Converter) breakwater [67]. Despite the same design parameters of the rotor with respect to the one investigated in this study (i.e., turbine solidity, hub-to-tip ratio and blade airfoil), they added inlet and outlet guide vanes and the numerical investigation is performed by means of URANS approach under steady inlet flow conditions; hence, the hysteretic

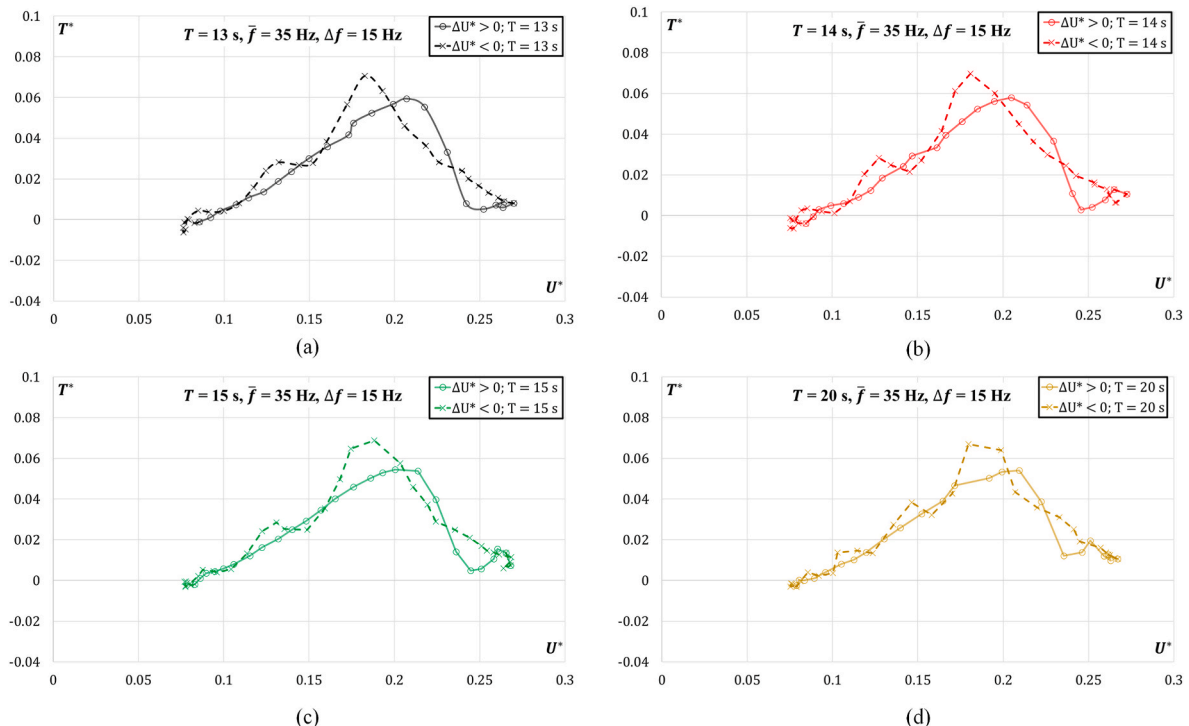


Fig. 21. Comparison between clockwise phase-averaged hysteresis loops for different periods in stall condition.

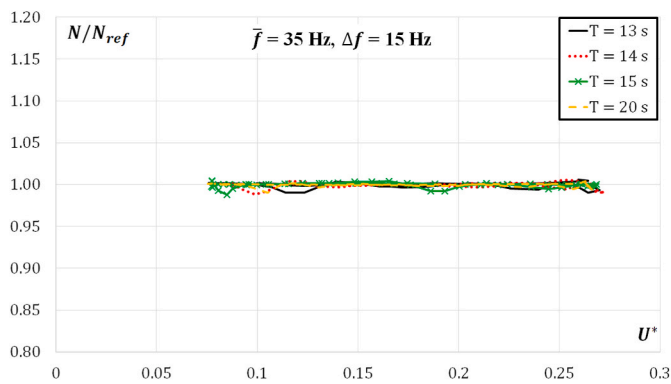


Fig. 22. Comparison between N/N_{ref} vs. U^* during hysteresis loops for different periods in stall condition.

behavior of the machine during stall is not evaluated. Indeed, the operating points of the machine under dynamic stall conditions do not always correspond to the ones retrieved under steady inlet flow conditions.

Finally, the rotational speed control has been analyzed, since the rotational speed of the machine is kept constant at 1750 rpm by means of a controller during cyclic working conditions (both under unstalled and deep stall phases). Fig. 22 compares the ratio between the instant value of the read rotational speed, N , and the reference value $N_{ref} = 1750$ rpm vs. the flow rate coefficient for all four periods. It is possible to notice how during hysteresis loops, the ratio N/N_{ref} remains within 1%.

6. Conclusions

In this work a monoplane Wells turbine has been investigated by carrying out an experimental campaign at the GaVe laboratory of the Polytechnic University of Bari, Italy. The aim of these tests was to investigate the behavior of this turbine under unsteady flow conditions, especially in terms of hysteresis loops during unstalled and dynamic stall conditions. Indeed, due to the oscillating nature of the flow rate in this kind of applications, Wells turbines are affected by dynamic stall, which has significant effects in terms of performance, fatigue, noise and structural integrity of the turbine. Actually, during stall the Wells turbine experiences evident torque fluctuations, which overlay on the typical hysteresis loop, mainly during flow deceleration. The amplitudes of these fluctuations are damped as the flow rate decreases toward reattachment. Often these fluctuations are not evident because hysteresis loops are usually provided with phase-averaged data, which can significantly smoothen or even conceal them.

With the aim to better investigate this phenomenon, this work proposes a 3D-printed monoplane Wells turbine, which has been tested at the open wind tunnel of the Polytechnic University of Bari, Italy. The novel contribution of this work consists in proposing a comprehensive experimental analysis of the machine working under cyclically varying flow conditions in order to highlight how the stall triggers this phenomenon. The interest is mainly focused on the effects of frequency, amplitude and period of the oscillating flow rate on the performance of the machine. In order to replicate typical unsteady working conditions in OWC systems, a unidirectional sinusoidal oscillating flow has been generated by varying the frequency signal sent to the vector control drive of the blower. The machine has been firstly investigated under steady state conditions, then under dynamic stall conditions. A total of 36 tests have been carried out by changing the three main parameters, which characterize the oscillating flow (i.e., the period, T , the mean frequency, \bar{f} , and the amplitude, Δf , of the frequency signal sent to the vector control drive).

The first study has been focused on finding out the period below which the flow rate does not follow the sinusoidal trend imposed by the

blower (i.e., $T = 13$ s). Then, a series of analyses has been carried out in order to evaluate the effect of a parameter, by keeping constant the other ones.

Different tests for unstalled working conditions have been carried out by proving that turbine shows its typical hysteresis loop which is not altered by torque oscillations even with flow coefficients close the stall condition without exceeding it. Then, the turbine is well controlled during the cyclic operating conditions.

Increasing the mean frequency or the frequency amplitude of the inverter involves the machine working towards stall condition, due to the increase of the flow rate. In addition, during dynamic stall, the shaft torque experiences damped fluctuations at frequencies higher than that of the main flow. This phenomenon happens during the flow deceleration and the flow reattachment. The torque coefficient shows a number of peaks during deceleration phases ranging from 2 to 4. Specifically, in correspondence of the case with the maximum period (i.e., $T = 20$ s) shows a greater number of peaks (4) than those relative to the other cases (about 3). Then, the greater number of peaks can be associated to the greater period in which a single cycle has to be completed.

Moreover, it has been found out how this unsteady behavior is not caused by both the mass flow rate crossing the turbine and the stagnation pressure drop. Indeed, these two performance parameters does not show perturbations or fluctuations over the period, resulting in a sinusoidal trend, as imposed by the blower. Moreover, the rotational speed control is performed correctly keeping the rotational speed within 1% of the target value. Actually, some works have tried to explain the behavior under deep stall condition by means of numerical simulations. Despite their valuable results, the numerical assessments were carried out under steady inlet flow conditions; hence, the hysteretic behavior of the machine during stall is not evaluated. Indeed, the operating points of the machine under dynamic stall conditions do not always correspond to the ones retrieved under steady inlet flow conditions.

Then, this experimental campaign can be used to understand the complex mechanisms behind the dynamic stall condition of a Wells turbine by means of unsteady numerical simulation aimed to simulate the entire hysteresis loop under dynamic stall condition. Finally, detecting these oscillations can be relevant in the turbine design phase to enhance the structural strength of the Wells turbine.

Funding

This research did not receive any specific grant from funding agencies in the public, commercial, or not-for-profit sectors.

CRediT authorship contribution statement

Michele Stefanizzi: Conceptualization, Methodology, Formal analysis, Investigation, Data curation, Writing – original draft, Writing – review & editing. **Sergio Mario Camporeale:** Conceptualization, Methodology, Formal analysis, Investigation, Writing – original draft, Writing – review & editing, Supervision. **Marco Torresi:** Writing – original draft, Methodology, Supervision.

Declaration of competing interest

The authors declare that they have no known competing financial interests or personal relationships that could have appeared to influence the work reported in this paper.

Acknowledgements

This work was partly supported by the Italian Ministry of University and Research under the Programme “Department of Excellence” Legge 232/2016 (Grant No. CUP - D93C23000100001) and partly supported under the National Recovery and Resilience Plan (NRRP), Mission 4 Component 2 Investment 1.3 - Call for tender No. 1561 of 11.10.2022 of

Ministero dell'Università e della Ricerca (MUR); funded by the European Union – NextGenerationEU. Project code PE0000021, Concession Decree No. 1561 of 11.10.2022 adopted by Ministero dell'Università e

della Ricerca (MUR), CUP - D93C22000900001, Project title “Network 4 Energy Sustainable Transition – NEST”.

Nomenclature

Symbols

c	Blade chord [m]
D	Diameter [m]
f	Frequency [Hz]
G	Mass flow rate [kg/s]
h	Hub-to-tip ratio [–]
N	Rotational speed [rpm]
N_b	Number of blades [–]
P	Power [W]
R_{hub}	Hub radius [m]
R_{tip}	Tip radius [m]
s	Solidity [–]
T	Period [s]
T^*	Torque coefficient [–]
V	Air axial velocity [m/s]
Δf	Frequency amplitude [Hz]
Δp^*	Stagnation pressure drop coefficient [–]

Greek letters

β	Orifice diameter ratio [–]
η	Efficiency [–]
ρ	Density [kg/m ³]
ω	Angular velocity [rad/s]

Abbreviations

CFD	Computational Fluid Dynamic
DOE	Design Of Experiments
LCOE	Levelized Cost of Energy
OWC	Oscillating Water Column
PTO	Power Take-Off
SCADA	Supervisor Control and Data Acquisition
TRL	Technology Readiness Level

References

- [1] International Energy Agency (IEA), CO2 Emissions in 2022, 2023. Url: <https://www.iea.org/reports/co2-emissions-in-2022>.
- [2] International Energy Agency (IEA), Global Energy & CO₂ Status Report 2019, IEA, Paris, France, 2019.
- [3] International Energy Agency (IEA), Global Energy Review 2020 - the Impacts of the COVID-19 Crisis on Global Energy Demand and CO₂ Emissions, IEA, Paris, France, 2020.
- [4] IEA, World Energy Outlook 2021, IEA, Paris, 2021, 2021, <https://www.iea.org/reports/world-energy-outlook-2021>.
- [5] UN Climate Change Conferene Egypt, 2022. Url: <https://cop27.eg/#/>.
- [6] T. Capurso, M. Stefanizzi, M. Torresi, S.M. Camporeale, Perspective of the role of hydrogen in the 21st century energy transition, Energy Convers. Manag. 251 (2022), 114898, <https://doi.org/10.1016/j.enconman.2021.114898>.
- [7] M. Stefanizzi, T. Capurso, G. Filomeno, M. Torresi, G. Pascazio, Recent combustion strategies in gas turbines for propulsion and power generation toward a zero-emission future: fuels, burners, and combustion techniques, Energies 14 (20) (2021) 6694, <https://doi.org/10.3390/en14206694>.
- [8] IRENA, Renewable Capacity Highlights, 2022.
- [9] IRENA, Offshore Renewables: an Action Agenda for Deployment, International Renewable Energy Agency, Abu Dhabi.
- [10] G. Mørk, S. Barstow, A. Kabuth, M. Pontes, Assessing the global wave energy potential, in: Proceedings of the 29th International Conference on Ocean, Offshore and Arctic Engineering, vol. 3, ASME, 2010, pp. 447–454.
- [11] European Union Commission, An EU Strategy to Harness the Potential of Offshore Renewable Energy for a Climate Neutral Future, 2020. https://ec.europa.eu/ener/sites/ener/files/offshore_renewable_energy_strategy.pdf.
- [12] S. Astariz, G. Iglesias, The economics of wave energy: a review, Renew. Sustain. Energy Rev. 45 (2015) 397–408, <https://doi.org/10.1016/j.rser.2015.01.061>.
- [13] Ocean Energy Europe, 2030 Ocean Energy Vision – Industry Analysis of Future Deployments, Cost and Supply Chains, 2020. https://www.oceanenergy-europe.eu/wp-content/uploads/2020/10/OEE_2030_Ocean_Energy_Vision.pdf.
- [14] Ocean Energy Europe, Ocean Energy – Key Trends and Statistics 2020, 2021. <https://www.oceanenergy-europe.eu/wp-content/uploads/2021/03/OEE-Stats-Trends-2020.pdf>.
- [15] M.A. Mustapa, O.B. Yaakob, Y.M. Ahmed, C.K. Rheem, K.K. Koh, F.A. Adnan, Wave energy device and breakwater integration: a review, Renew. Sustain. Energy Rev. 77 (2017) 43–58, <https://doi.org/10.1016/j.rser.2017.03.110>.
- [16] İ.Ö. Erselcan, D. Özkan, E. Sulukan, T.S. Uyar, Wave energy conversion technologies, in: T.S. Uyar, N. Javani (Eds.), Renewable Energy Based Solutions, Lecture Notes in Energy, vol. 87, Springer, Cham, 2022, https://doi.org/10.1007/978-3-031-05125-8_14.
- [17] A.K. Güths, P.R.F. Teixeira, E. Didier, A novel geometry of a onshore Oscillating Water Column wave energy converter, Renew. Energy 2021 (2022) 938–949, <https://doi.org/10.1016/j.renene.2022.10.121>.
- [18] B.A. Kharkeshi, R. Shafaghat, K. Rezanejad, R. Alamian, Measuring and investigating the effect of sloshing on the performance of a OWC wave energy converter by means of a novel experimental approach, Ocean Eng. 275 (2023), 114130, <https://doi.org/10.1016/j.oceaneng.2023.114130>.
- [19] H. Ding, J. Zang, P. Jin, D. Ning, X. Zhao, Y. Liu, C. Bleinkinsopp, Q. Chen, Optimization of the hydrodynamic performance of a wave energy converter in an integrated cylindrical wave energy converter-type breakwater system, J. Offshore Mech. Arctic Eng. 145 (5) (2023), 05450, <https://doi.org/10.1115/1.4056942>.
- [20] Z. Wang, S. Wu, K.H. Lu, Improvement of stability in an oscillating water column wave energy using an adaptive intelligent controller, Energies 16 (1) (2022) 133, <https://doi.org/10.3390/en16010133>.
- [21] C. Yang, T. Xu, C. Wan, H. Liu, Z. Su, L. Zhao, H. Chen, L. Johanning, Numerical Investigation of a dual cylindrical OWC hybrid system incorporated into a fixed caisson breakwater, Energy 263 (2023), 126132, <https://doi.org/10.1016/j.energy.2022.126132>.

- [22] S. El Bouji, N. Kamil, Z. Beidouri, Experimental study of an oscillating water column wave energy converter based on regular waves, *Mar. Syst. Ocean Technol.* 17 (2023) 147–163, <https://doi.org/10.1007/s40868-022-00121-2>.
- [23] D. Zhang, C.Z. Chen, X. Liu, J. Sun, H. Yu, W. Zeng, Y. Ying, Y. Sun, L. Cui, S. Yang, P. Qian, Y. Si, A coupled numerical framework for hybrid floating offshore wind turbine and oscillating water column wave energy converters, *Energy Convers. Manag.* 267 (2022), 115933, <https://doi.org/10.1016/j.enconman.2022.115933>.
- [24] I. Ahmad, F. M'zoughi, P. Aboutalebi, I. Garrido A.J. Garrido, A regressive A regressive machine-learning approach to the non-linear complex FAST model for hybrid floating offshore wind turbines with integrated oscillating water columns, *Sci. Rep.* 13 (2023) 1499, <https://doi.org/10.1038/s41598-023-28703-z>.
- [25] I. Simonetti, A. Esposito, L. Cappiotti, Experimental proof-of-concept of a hybrid wave energy converter based on oscillating water column and overtopping mechanisms, *Energies* 15 (21) (2023) 8065, <https://doi.org/10.3390/en15218065>.
- [26] S. Raghunathan, The wells air turbine for wave energy conversion, *Prog. Aero. Sci.* 31 (4) (1995) 335–386, [https://doi.org/10.1016/0376-0421\(95\)00001-F](https://doi.org/10.1016/0376-0421(95)00001-F).
- [27] *Ocean Wave Energy Systems – Hydrodynamics, Power Takeoff and Control Systems*, Springer, 2022, <https://doi.org/10.1007/978-3-030-78716-5>.
- [28] E. Medina-Lopez, N.W.H. Allsop, A. Dimakopolus, T. Bruce, Conjectures on the failure of the OWC breakwater at Mutriku, in: *Proceedings of Coastal Structures and Solutions to Coastal Disasters Joint Conference*, 2015. Boston, Massachusetts.
- [29] Y. Torre-Enciso, I. Ortubia, L.I. López de Aguilera, J. Marqués, Mutriku wave power plant: from the thinking out to the reality, in: *Proceedings of the 8th European Wave and Tidal Energy Conference*, 2009, 19329. Uppsala, Sweden.
- [30] Wikipedia, Mutriku Breakwater Wave Plan. Url https://en.wikipedia.org/wiki/Mutriku_Breakwater_Wave_Plan [online, access on 20/07/2022].
- [31] Offshore energy, Mutriku Wave Plant Hits 2 GWh Mark. Url: <https://www.offshore-energy.biz/mutriku-wave-plant-hits-2gwh-mark/> [online, access on 20/07/2022].
- [32] A.F.O. Falcão, J.C.C. Henriques, Oscillating-water-column wave energy converters and air turbines: a review, *Renew. Energy* 85 (2016) 1391–1424, <https://doi.org/10.1016/j.renene.2015.07.086>.
- [33] W.M.L. Monteiro, A. Sarmento, C.P. Monteiro, J.A.L. Monteiro, Wave energy production by a maritime Natural Cave: performance characterization and the power take-off design, *J. Ocean Eng. Mar. Energy* 7 (2021) 327–337, <https://doi.org/10.1007/s40722-021-00196-w>.
- [34] R. Abassi, M.J. Ketabdari, Enhancement of OWC Wells turbine efficiency and performance using riblets covered blades, a numerical study, *Energy Convers. Manag.* 254 (2022), 1152212, <https://doi.org/10.1016/j.enconman.2022.115212>.
- [35] L.M.C. Gato, V. Warfield, A. Thakker, Performance of a high-solidity wells turbine for an OWC wave power plant, *J. Energy Resour. Technol.* 118 (4) (1996) 263–268, <https://doi.org/10.1115/1.2793872>.
- [36] M. Takao, K. Takasaki, S. Okuhara, T. Setoguchi, Wells turbine for wave energy conversion- improvement of stall characteristics by the use of 3-dimensional blades, *J. Fluid Sci. Technol.* 9 (2014) 1–7, <https://doi.org/10.1299/jfst.2014jfst0052>.
- [37] M. Torresi, S.M. Camporeale, P.D. Strippoli, G. Pascasio, Accurate numerical simulation of a high solidity Wells turbine, *Renew. Energy* 33 (2008) 735–747, <https://doi.org/10.1016/j.renene.2007.04.006>.
- [38] A.T.M. Kotb, M.A.A. Nawar, R.A. El Maksoud, Y.A. Attai, M.H. Mohamed, Potential of performance improvement of a modified Wells turbine using passive control for wave energy conversion, *Ocean Eng.* 242 (2021), 110178, <https://doi.org/10.1016/j.oceaneng.2021.110178>.
- [39] A.T.M. Kotb, M.A.A. Nawar, Y.A. Attai, M.H. Mohamed, Performance assessment of a modified wells turbine using an integrated casing groove and Gurney flap design for wave energy conversion, *Renew. Energy* 197 (2022) 627–642, <https://doi.org/10.1016/j.renene.2022.07.140>.
- [40] K. Geng, C. Yang, C. Hu, Y. Li, C. Yang, Numerical investigation on the loss audit of Wells turbine with exergy analysis, *Renew. Energy* 189 (2022) 273–287, <https://doi.org/10.1016/j.renene.2022.02.042>.
- [41] L. Ciappi, L. Cheli, I. Simonetti, A. Bianchini, L. Talluri, L. Cappiotti, G. Manfrida, Wave-to-wire models of wells and impulse turbines for oscillating water column wave energy converters operating in the Mediterranean Sea, *Energy* 238 (2022), 121585, <https://doi.org/10.1016/j.energy.2021.121585>.
- [42] L. Ciappi, L. Cheli, I. Simonetti, A. Bianchini, G. Manfrida, L. Cappiotti, Wave-to-wire models of oscillating-water-column wave energy converters and its applications to mediterranean energy hot-spots, *Energies* 13 (21) (2020) 5582, <https://doi.org/10.3390/en13215582>.
- [43] L. Gurnari, P.G.F. Filianoti, M. Torresi, S.M. Camporeale, The wave-to-wire energy conversion process for a fixed U-OWC device, *Energies* 13 (1) (2020) 283, <https://doi.org/10.3390/en13010283>.
- [44] S. Shaaban, A.A. Hafiz, Effect of duct geometry on Wells turbine performance, *Energy Convers. Manag.* 61 (2012) 51–58, <https://doi.org/10.1016/j.enconman.2012.03.023>.
- [45] J.S. Alves, L.M.C. Gato, A.F.O. Falcão, J.C.C. Henriques, Experimental investigation on performance improvement by mid-plane guide-vanes in a biplane-rotor Wells turbine for wave energy conversion, *Renew. Sustain. Energy Rev.* 150 (2021), 111497, <https://doi.org/10.1016/j.rser.2021.111497>.
- [46] A. Mahrooghi, E. Lakzian, Optimization of Wells turbine performance using a hybrid artificial neural fuzzy inference system (ANFIS) - genetic algorithm (GA), *Ocean Eng.* 226 (2021), 108861, <https://doi.org/10.1016/j.oceaneng.2021.108861>.
- [47] R. Starzmann, T. Carolus, Effect of blade skew strategies on the operating range and aeroacoustic performance of the wells turbine, *J. Turbomach.* 136 (1) (2014), 011003, <https://doi.org/10.1115/1.4025156>.
- [48] P.M. Kumar, P. Halder, A. Husain, A. Samad, Performance enhancement of Wells turbine: combined radiused edged blade tip, static extended trailing edge, and variable thickness modifications, *Ocean Eng.* 185 (2019) 47–58, <https://doi.org/10.1016/j.oceaneng.2019.05.041>.
- [49] M. Paderi, P. Puddu, Experimental investigation in a Wells turbine under bidirectional flow, *Renew. Energy* 57 (2013) 570–576.
- [50] P. Puddu, M. Paderi, C. Manca, Aerodynamic characterization of a Wells turbine under bi-directional airflow, *Energy Proc.* 45 (2014) 278–287.
- [51] T. Setoguchi, Y. Kinoue, T.H. Kim, K. Kaneko, M. Inoue, Hysteretic characteristics of Wells turbine for wave power conversion, *Renew. Energy* 28 (13) (2003) 2113–2127.
- [52] A. Thakker, R. Abdulhadi, Effect of blade profile on the performance of wells turbine under unidirectional sinusoidal and real sea flow conditions, *Int. J. Rotating Mach.* (2007), 51598.
- [53] A. Thakker, R. Abdulhadi, The performance of Wells turbine under bi-directional airflow, *Renew. Energy* 33 (11) (2008) 2467–2474.
- [54] T.H. Kim, Y. Kinoue, T. Setoguchi, K. Kaneko, Effects of hub-to-tip ratio and tip clearance on hysteretic characteristics of wells turbine for wave power conversion, *J. Therm. Sci.* 11 (3) (2002) 207–213.
- [55] F. Licheri, T. Ghisu, F. Cambuli, P. Puddu, Wells turbine efficiency improvements: experimental application of a speed control strategy, *J. Phys. Conf.* 2385 (2022), 012132, <https://doi.org/10.1088/1742-6596/2385/1/012132>.
- [56] F. Licheri, T. Ghisu, F. Cambuli, P. Puddu, Detailed investigation of the local flow-field in a Wells turbine coupled to an OWC simulator, *Renew. Energy* 197 (2022) 583–593, <https://doi.org/10.1016/j.renene.2022.07.116>.
- [57] T. Setoguchi, Y. Kinoue, M. Mohammad, K. Kaneko, M. Takao, Unsteady flow phenomena of Wells turbine in deep stall condition, in: *Proceedings of the 14th International Offshore and Polar Engineering Conference*, Toulon, France, 2004, pp. 266–271.
- [58] T. Ghisu, P. Puddu, F. Cambuli, Physical explanation of the hysteresis in Wells turbines: a critical reconsideration, *J. Fluid Eng.* 138 (11) (2016) 1–9.
- [59] F. M'zoughi, I. Garrido, A.J. Garrido, M. De La Sen, Rotational speed control using ANN-based MPPT for OWC based on surface elevation measurement, *Appl. Sci.* 10 (24) (2020) 8975, <https://doi.org/10.3390/app10248975>.
- [60] Y. Kinoue, T. Setoguchi, T.H. Kim, M. Mammum, K. Kaneko, M. Inoue, Hysteretic characteristics of the Wells turbine in a deep stall condition, *Proc. IME M J. Eng. Marit. Environ.* 218 (3) (2004) 167–173, <https://doi.org/10.1243/147509004173796>.
- [61] R. Starzmann, T.H. Carolus, K. Tease, R. Arlitt, Effect of design parameters on aero-acoustic and aerodynamic performance of Wells turbines, in: *Proceedings of the ASME 2011 30th International Conference on Ocean, Offshore and Arctic Engineering*, 2011, pp. 299–308, <https://doi.org/10.1115/OMAE2011-491270>.
- [62] P. Puddu, M. Paderi, C. Manca, Aerodynamic characterization of a wells turbine under Bi-directional airflow, *Energy Proc.* 45 (2014) 278–287, <https://doi.org/10.1016/j.egypro.2014.01.030>.
- [63] Q. Hu, Y. Li, Unsteady RANS simulations of wells turbine under transient flow conditions, *J. Offshore Mech. Arctic Eng.* 140 (1) (2017), 011901, <https://doi.org/10.1115/1.4037696>.
- [64] T. Ghisu, F. Cambuli, P. Puddu, I. Virdis, M. Carta, F. Licheri, A critical examination of the hysteresis in wells turbines using computational Fluid dynamics and lumped parameter models, *J. Offshore Mech. Arctic Eng.* 142 (5) (2020), 052001, <https://doi.org/10.1115/1.4046379>.
- [65] K. Geng, C. Yang, X. He, C. Hu, H. Zhang, X. Shi, Circulation budget analysis of the leading-edge vortex in a wells turbine under steady inflow conditions, Rotterdam, Netherlands. June 13–17, in: *Proceedings of the ASME Turbo Expo 2022: Turbomachinery Technical Conference and Exposition, Turbomachinery — Axial Flow Turbine Aerodynamics; Deposition, Erosion, Fouling, and Icing; Radial Turbomachinery Aerodynamics*, 10B, 2022, https://doi.org/10.1115/GT2022-81890_V10BT30A014.
- [66] K. Geng, C. Yang, H. Zhang, B. Zhao, C. Hu, J. Gao, Y. Li, Influence of vortex interactions on the exergy transfer and performance of OWC Wells turbine, *Proc. Inst. Mech. Eng. A J. Power Energy* (2023), <https://doi.org/10.1177/09576509231163390>.
- [67] S.M. Camporeale, P.G.F. Filianoti, Energy Conversion of OWC devices with additional vertical ducts, in: *Proceedings of the 27th International Conference of Offshore Mechanics and Arctic Engineering*, 2008, pp. 739–750, <https://doi.org/10.1115/OMAE2008-57769>.
- [68] M. Torresi, M. Stefanizzi, L. Gurnari, P.G.F. Filianoti, S.M. Camporeale, Experimental characterization of the unsteady performance behavior of a Wells Turbine operating at high flow rate coefficients, in: *E3S Web of Conferences*, vol. 197, 2020, 08009, <https://doi.org/10.1051/e3sconf/202019708009>.
- [69] M. Torresi, M. Stefanizzi, F. Fornarelli, L. Gurnari, P.G.F. Filianoti, S. M. Camporeale, Performance characterization of a Wells turbine under unsteady flow conditions, *AIP Conf. Proc.* 2191 (2019), 020149, <https://doi.org/10.1063/1.5138882>.
- [70] R.E. Sheldahl, P.C. Klimas, Aerodynamic Characteristics of Seven Symmetrical Airfoil Sections through 180-degree Angle of Attack for Use in Aerodynamic Analysis of Vertical axis Wind Turbines, Sandia National Laboratories Energy Report, 1981, <https://doi.org/10.2172/6548367>.
- [71] W.J. McCroskey, The phenomenon of dynamic stall, *Tech. Memorandum* 81264, Natl. Aeronaut. Space Admin, Washington, DC, 1981, pp. 1–28. <https://ntrs.nasa.gov/api/citations/19810011501/downloads/19810011501.pdf>.
- [72] M. Torresi, E. De Tomaso, B. Fortunato, S.M. Camporeale, G. Pascasio, High frequency dynamics of force coefficients in VAWT blades under dynamic stall condition, in: *The Proceedings of ASME Turbo Expo 2015: Power for Land, Sea and Air*, 2015, pp. GT2015-42987, <https://doi.org/10.1115/GT2015-42987>.